Analysis of strain in the {11$\bar{2}$0} prismatic fault in GaN using digital processing of high-resolution transmission electron microscopy images

2000 J. Phys.: Condens. Matter 12 10249

(http://iopscience.iop.org/0953-8984/12/49/325)

J. Phys.: Condens. Matter **12** (2000) 10249–10256. Printed in the UK PII: S0953-8984(00)17891-9

Analysis of strain in the $\{11\bar{2}0\}$ prismatic fault in GaN using digital processing of high-resolution transmission electron microscopy images

S Kret, P Ruterana and G Nouet

ESCTM-CRISMAT UMR 6508, CNRS-ISMRA, 6 Boulevard du Maréchal Juin, 14050 Caen Cédex, France

Received 10 October 2000

Abstract. Using the geometric phase method and measurements of dislocation core distributions, a quantitative analysis of the contrast exhibited by [0001] HRTEM images of the $\{11\bar{2}0\}$ prismatic stacking fault in GaN was carried out. Such analysis allows precise determination of the displacement vector and location of any additional defects inside the boundary, such as steps and dislocations. For relaxed segments, a perfect matching between experimental and simulated images based on the Drum model was obtained. When stress fields are present, the deviation of the atomic structure of the boundary from the theoretical models is significant. Lattice reconstruction inserts fragments of additional planes in the boundary and dislocations are revealed.

1. Introduction

During growth of GaN wurtzite structure (2H) epilayers on various substrates, planar faults can be generated at interfaces [1, 2]. Previous results have shown that the $\{11\bar{2}0\}$ prismatic stacking fault is the most common at the GaN/6H-SiC interface [3]. Agreement between the calculated structure and high-resolution observations was found for relaxed segments of these faults when the Drum atomic model was considered [3–5]. The atomic structure of these defects was reconstructed using the Stillinger–Weber potential and the total displacement vector perpendicular to the fault plane was determined to be close to $0.53a$ [6].

In this study we show that the strain fields generated during coalescence of islands may lead to prismatic faults with dislocations in the boundary plane. Quantitative strain determination associated with the measurement of dislocation core distributions by the digital processing of HRTEM images helps us to interpret this structural variation [7].

2. Experimental details and digital processing procedure

The plan-view [0001] TEM samples of GaN epilayers on SiC substrate were prepared in the conventional way by mechanical polishing followed by ion milling. HRTEM was carried out on a Topcon 002B microscope operating at 200 kV with a point resolution of 0.18 nm. The HRTEM images were formed by using only $01\bar{1}0$-type diffracted beams with weak contributions from $11\bar{2}0$ beams. Images used in this study were recorded on photographic films and digitized, sampling at 0.15 Å/pixel and with an 8-bit dynamic. Image simulations for the perfect crystals and defect structures were performed using the EMS package [8].

0953-8984/00/4910249+08$30.00

These simulations help us to select images in which the simple interpretation of contrast features is possible. In the micrographs analysed, bright spots correspond to tunnels in the [0001] projection. Simulations show that even for defects, the deviations of the observed image contrast from the projected structure are negligibly small under these conditions [4]. Processing of experimental images was performed using routines written in ALI (analytical language for images) in the Optimas graphical environment [9].

Our procedure starts with analysis of individual image periodicity by using the geometric phase method [10]. The raw phase images $P'_g(z_1, z_2)$ and $P_g(z_1, z_2)$ related to perfect-structure phase images are calculated for $10\bar{1}0$, $01\bar{1}0$, and $1\bar{1}00$ lattice periodicity. The local coordinate system was chosen for the analysis of particular parts of prismatic faults: the z_1- and z_2-axes are parallel and perpendicular to the defect boundary respectively, and the z_3-axis is always perpendicular to the image plane. Next, the lattice displacement field $\hat{\boldsymbol{u}}(z_1, z_2)$ has been calculated using the following vector relation:

$$P_{gi}(z_1, z_2) = -2\pi \boldsymbol{g}_i \cdot \hat{\boldsymbol{u}}(z_1, z_2).$$

By differentiation of the displacement field $\hat{\boldsymbol{u}}(z_1, z_2)$, the lattice distortion tensor $\beta_{ij}(z_1, z_2)$ was deduced. Then, the dislocation core distribution tensor

$$\tilde{\boldsymbol{\alpha}} \stackrel{\mathrm{d}f}{=} -\mathrm{curl}\,\boldsymbol{\beta}$$

and in-plane Burgers vector components

$$\hat{\boldsymbol{b}} = -\int_{S_c} \tilde{\boldsymbol{\alpha}}\,\mathrm{d}s$$

(S_c is the dislocation core surface) were determined by applying the formalism of the continuum theory of dislocations [7].

The presence of the fault boundary can introduce the lattice shift in the z_2-direction related to the perfect lattice of GaN. This lattice shift is calculated as

$$\mathrm{Ls}(z_1) = \int \beta_{22}(z_1, z_2)\,\mathrm{d}z_2$$

near the interface region, as a function of the boundary position z_1. The integration was performed along the frame width (figure 1) for each position z_1, and in this way the variation of $\mathrm{Ls}(z_1)$ was extracted along the boundary.

The calculated $\mathrm{Ls}(z_1)$ value contains the fault R_f-vector and the additional lattice shift connected with atomic structure relaxation, influenced by external strains introduced by nearby defects (islands, amorphous domain threading, dislocations, etc). The difference $(\mathrm{Ls}(z_1) - R_f)$ gives the perpendicular boundary expansion of the fault.

3. Results

Figure 1 shows an image with two non-parallel (60°-oriented) parts of a $\{11\bar{2}0\}$ prismatic fault. The first one is connected to an amorphous domain and the second is terminated by a partial dislocation. Enlarged images of the boundary are shown in figures 2(a) and 3(a). It is clear that the structure of SF1 changes from the amorphous domain to the other end. The changes in the SF2 part are even more important: we can clearly distinguish three segments. Segments A and C have similar structure whereas segment B may be compared to SF1.

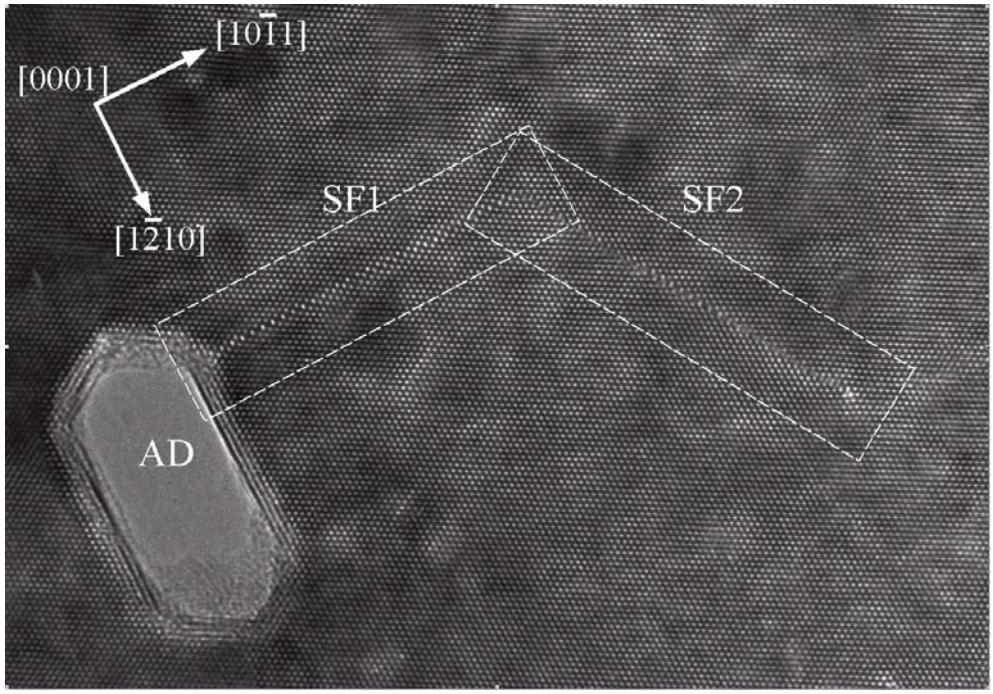

Figure 1. A high-resolution image in [0001] projection of a $\{11\bar{2}0\}$ prismatic stacking fault associated with an amorphous domain.

3.1. Structure analysis of SF1

Previous work [3, 11] showed that the fault boundary which is close to the amorphous domain corresponds very well to the Drum atomic model. In this model the atomic planes $(01\bar{1}0)$ perpendicular to the fault interface cross it without deviation. The raw phase images for $01\bar{1}0$ periodicity (figure 2(d)) shows that this feature holds along the entire boundary. However, the $(1\bar{1}00)$ and $(10\bar{1}0)$ planes are highly distorted, especially in the region of contact with SF2.

The units cells used for analysing the HRTEM micrograph are based on the white dots corresponding to tunnels in the GaN [0001] projection or the tunnel between eight atoms of the interface in the Drum model. This means that only one unit cell crossing the interface measured on an HRTEM micrograph will be extended by 50% (distortion $\beta = 0.5$) compared to the reference lattice. However, the atomistic simulations showed that neighbouring atomic plane distances can be modified too, and the total perpendicular boundary shift can be larger than that predicted by the geometric model [3]. The measurement of the lattice distortion tensor $\boldsymbol{\beta}$ can be used to verify these assumptions.

The $\beta_{22}(z_1, z_2)$ component maps (figure 2(e)) show that the lattice distances near the fault interface are expanded in the z_2-direction as compared to the perfect crystal. Using this map, the total interface width (where the lattice distances differ from the reference lattice) can be directly measured. In the case of SF1 the interface width varies between $5a$ and $7a$. The measured maximum value of $\beta_{22}(z_1, z_2)$ varies from 0.2 to 0.42 and does not reach the theoretical value of 0.5 derived from the Drum model.

In contrast, the measurement of total perpendicular boundary shift always gives a value larger than $0.5a$. We find $\mathrm{Ls} = 0.53a$ near the amorphous domain. This value is very

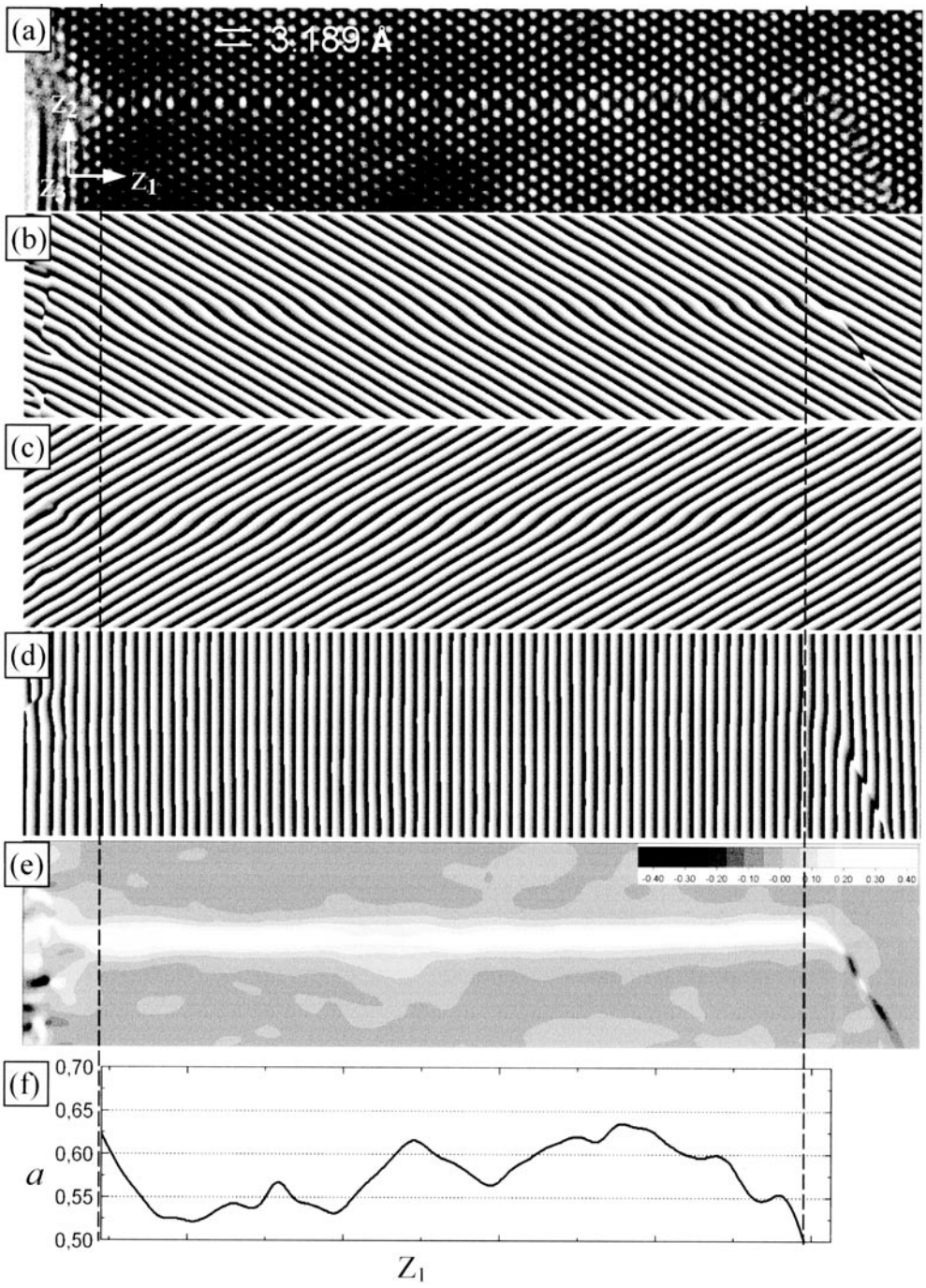

Figure 2. (a) Frame SF1 of figure 1 with a local coordinate system; (b), (c), (d) raw phase images obtained respectively with lattice periodicity $10\bar{1}0$, $01\bar{1}0$, $1\bar{1}00$; (e) a map of the β_{22}-component of the distortion field; (f) the variation of the total boundary shift $\mathrm{Ls}(z_1)$ in units of a.

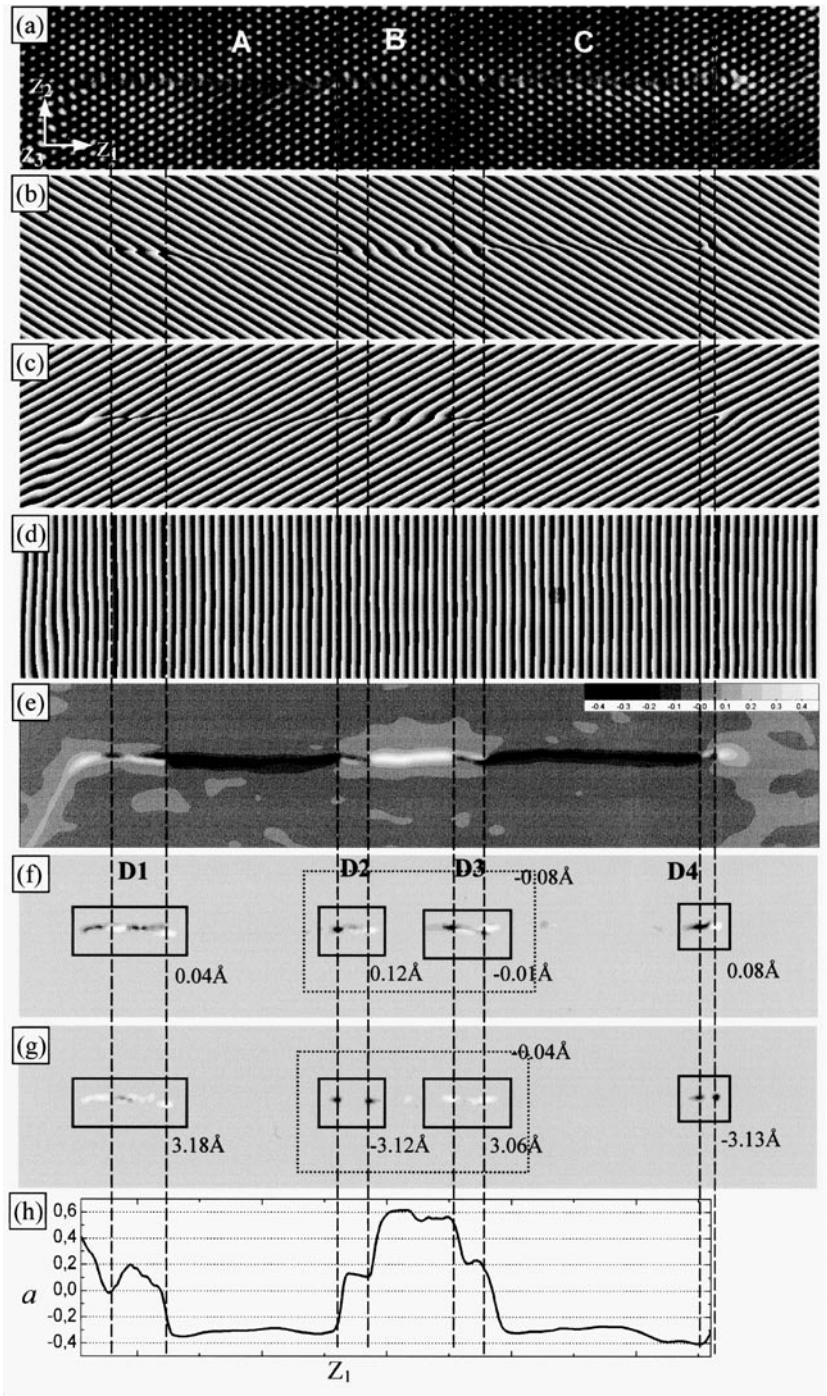

Figure 3. (a) Frame SF2 of figure 1 with a local coordinate system; (b), (c), (d) raw phase images obtained respectively with lattice periodicity $10\bar{1}0$, $01\bar{1}0$, $1\bar{1}00$; (e) a map of the β_{22}-component of the distortion field; (f), (g) α_{13}- and α_{23}-components of the dislocation core distribution field; (h) variation of the fault lattice shift $\mathrm{Ls}(z_1)$ in units of a.

close to the fault vector magnitude previously determined for the perfect Drum atomic model by atomistic simulations [6]. Nevertheless, the measured value changes along the boundary plane and can reach $0.65a$ as shown in figure 2(f). This means that the boundary expansion $(\mathrm{Ls}(z_1) - R_f)$ varies between 0.03 and $0.15a$.

3.2. Structure analysis of SF2

Similarly to the case for SF1, the atomic planes perpendicular to the fault do not deviate (figure 3(d)). The raw phase images shown in figures 3(b) and 3(c) clearly reveal interface dislocations as shown by the appearance of additional lattice planes. Close inspection of the images of segments A and C allows one to establish that an additional row of image maxima is present in the boundary, as can been seen in figure 4(c), which means that additional $(\bar{1}\bar{1}20)$ atomic planes are present.

The β_{22}-component maps (figure 3(e)) clearly show that these additional planes are highly compressed. The maximal negative distortion is between -0.15 and -0.22. The total boundary width of these segments does not exceed $(3–4)a$. Nevertheless, the distortion of segment B has positive values with maxima near +0.5. The total boundary width is similar to that measured for SF1.

By definition, the dislocation core distribution tensor $\boldsymbol{\alpha}$ takes non-zero values only near dislocation cores. Experimentally, it was shown that for a perfect dislocation with a compact core, the α-peak has a width nearly equal to one Burgers vector [7].

The dislocation core distribution tensor components α_{13} and α_{23} (figures 3(f) and 3(g)) clearly show that dislocations are grouped in pairs (D2, D3, and D4) or more complex structures like D1 where four α-peaks can be distinguished. Cores of the elementary dislocations are not compact: broadening of α-peaks is observed for many unit cells. The interaction length can be directly measured in the figures 3(f), 3(g) as the maximal spreading between dislocation core distribution peaks. The lengths of D1, D2, D3, and D4 are 14, 9, 8.5, and 4 Å respectively.

Integration of core distribution tensor components α_{13} over areas near dislocation cores gives the $\hat{b}_1$, in-plane Burgers components parallel to the fault interface. The perpendicular components $\hat{b}_2$ can be obtained by the integration of α_{23}. The rectangular frames on figures 3(f) and 3(g) show the integration surface. The numbers near the frames are the moduli of in-plane Burgers components which are obtained from integration. All four dislocation groups D1–D4 are in-plane total Burgers vectors of the type $(1/3)\langle 11\bar{2}0\rangle$ and the moduli of $\hat{b}_2$-components obtained are very close to $a = 3.18$ Å. D1 and D3 have effective Burgers vectors in opposite directions to those of structures D2 and D4. D2 and D3 form a dislocation dipole.

Parallel components $\hat{b}_1$ for each group of dislocations are very close to zero (0.01–0.13 Å). The deviation from theoretical values of Burgers vectors can be explained if a local rotation of the crystal lattice is considered.

The error bars on the calculated Burgers vectors for the dislocation groups D1 and D3 are difficult to estimate. Due to the core distribution, it is not easy to determine the surface of the cores of these dislocations, and only approximate values of Burgers vector moduli are obtained through integration. The dislocations in D4 have more compact cores and the Burgers vector moduli can be precisely determined as $(1/3)\langle 2\bar{1}\bar{1}0\rangle$ and $(1/3)\langle \bar{1}2\bar{1}0\rangle$.

For segments A and C of SF2, the measured total perpendicular boundary shift Ls is about $-0.35a$. On the other hand Ls for B is $(0.55–0.6)a$. It seems that the lattice extension of segment B is compensated by the introduction of additional planes in the A and C segments. This balance can be written as

$$(2a - 0.35a) \simeq (a + 0.55a).$$

A corresponding simplified model of SF2 is shown in figure 4.

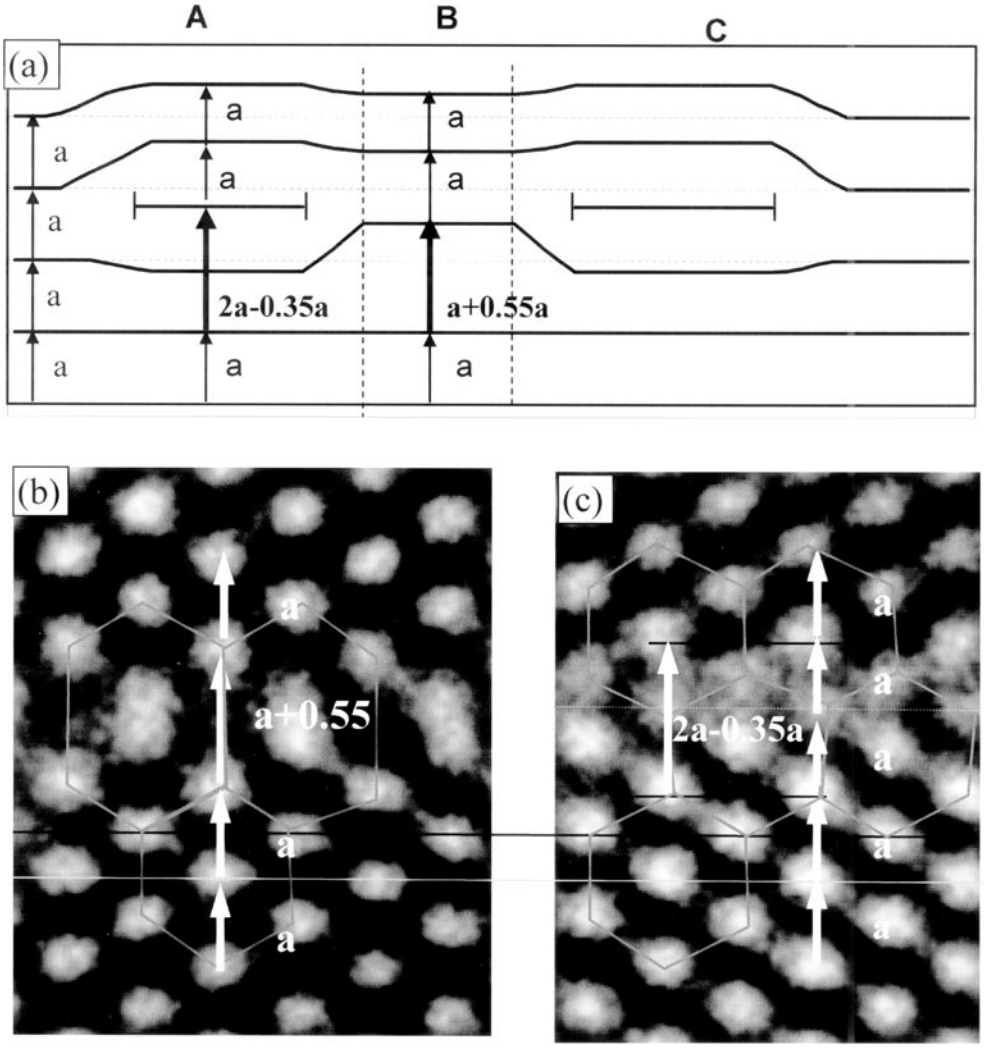

Figure 4. (a) A schematic model of the atomic plane configuration of the SF2 boundary. (b) Experimental HRTEM micrographs of the B segment. (c) Experimental HRTEM micrographs showing A and C segments with an additional lattice plane.

4. Conclusions

Local lattice distortion measurements by means of digital processing of HRTEM images associated with dislocation core distribution mapping is a fast and efficient tool for analysing the structure of defects. Our approach is faster and gives additional information about dislocation cores as compared to the conventional 2D circuit mapping. The resolution obtained is sufficient for detecting very short distances between dislocations. Quantitative measurement of the lattice distortion has allowed us to interpret the contrast variation in $\{11\bar{2}0\}$ prismatic stacking faults. It was found that the total perpendicular boundary expansion can change from $0.03a$ to $0.15a$. More work is needed in order to understand the fine structure of these defects and to determine their formation mechanisms.

Acknowledgment

This work was supported by the EC under contract HPRN-CT-1999-00040

References

[1] Tanaka S, Kern R S and Davis R F 1995 *Appl. Phys. Lett.* **66** 37
[2] Sverdlov B N, Martin G A, Morkoç H and Smith D J 1995 *Appl. Phys. Lett.* **67** 2063
[3] Vermaut P, Ruterana P, Nouet G and Morkoç H 1997 *Phil. Mag.* A **75** 239
[4] Vermaut P, Ruterana P and Nouet G 1997 *Phil. Mag.* A **76** 1215
[5] Drum C M 1965 *Phil. Mag.* A **11** 313
[6] Vermaut P, Béré A, Ruterana P, Nouet G, Hairie A and Paumier E 1998 *Thin Solid Films* **319** 153
[7] Kret S, Dłużewski P, Dłużewski P and Sobczak E 2000 *J. Phys.: Condens. Matter* **12**
[8] Stadelman P 1987 *Ultramicroscopy* **21** 131
[9] *Optimas 6.5 User Guide and Technical Reference* 1999 Media Cybernettics
[10] Hÿtch M J, Snoeck E and Killaas R 1998 *Ultramicroscopy* **74** 131
[11] Vermaut P, Nouet G and Ruterana P 1999 *Appl. Phys. Lett.* **74** 694